A VALIDATION STUDY USING NREL PHASE VI EXPERIMENTS, PART I: LOW COMPUTATIONAL RESOURCE SCENARIO

A. Aksenov[1] – U. Ozturk[2] – C.Yu P.[3] – Byvaltsev[1] – S. Soganci[4] – O. Tutkun[5]*

[1] Russian Academy of Sciences (JIHT RAS), Moscow, Russia
[2] ETSEIB, Universitat Politecnica de Catalunya, Av. Diagonal, 647, 08028 Barcelona, Spain, utkudeniz.ozturk@upc.edu
[3] Samwells, New Taipei City, Taiwan
[4] Capvidia NV, Leuven, Belgium
[5] Akana, Ankara, Turkey

*Corresponding Author

ABSTRACT

CFD calculations of NREL Phase VI rotor under wide range of operation conditions were conducted using FlowVision software. Computations were performed for various wind speeds with axial inflow, constant RPM and constant blade pitch.

The rotation of the blades was modeled via different approaches; steady-state with frozen rotor using rotating reference frame and transient with moving boundaries or sliding surfaces. In addition to this, an 'Overlapping Boundary Layer (OBL)' was implemented to resolve the boundary layer for a selected case. Turbulence models 'k-ε-AKN and k-ω Shear Stress Transport (SST) were used and compared. Except the OBL case, FlowVision wall function approximation was employed for all calculations with y+ values between 30 and 100.

Overall results were compared for all of the above-mentioned numerical approaches and showed good agreement with the experimental data. k-ω SST turbulence model is found to perform better to predict stall onset. The stall occurrence and general torque trend as a function of wind speed is fairly well captured. Comparisons of the static pressure distribution around blades with experimental data at different span-wise sections for different wind speeds are presented and good agreement is observed.

KEYWORDS: CFD, validation, FlowVision, Wind Turbine, NREL Phase VI, Stall Prediction

NOMENCLATURE

CFD	Computational Fluid Dynamics
RPM	Revolutions per Minute
HAWT	Horizontal Axis Wind Turbine
BEM	Beam Element Method
UAE	Unsteady Aerodynamics Experiments
RANS	Reynolds Averaged Navier-Stokes
NASA	the National Aeronautics and Space Administration
CAD	Computer Aided Drawing
DNS	Direct Numerical Simulation
CFL	Courant-Friedrichs-Lewy
NS	Navier-Stokes
MRF	Moving Reference Frame

INTRODUCTION

According to the Renewable Energy Policy Network's latest report (2015) energy consumption related carbon emissions has remained constant in 2014 despite a global increase in the energy use, highlighting the importance of renewable energy. Moreover, the share of overall electricity production via renewable sources in the global production is expected to rise from 18% (2010) to 30% by 2030.

Horizontal Axis Wind Turbines (HAWTs) are the most commonly used, complex energy harvesting systems where many sub-systems (bearings, gearbox etc.) work together in an integrated manner. Overall aerodynamic characteristics of the wind turbine influence the loading on the main and above-mentioned secondary elements. Since the topological and meteorological characteristics of the site where these systems are to be constructed should be considered upon the design (for instance through a Weibull distribution of frequency of wind speeds), aerodynamic design of the turbine is limited by many factors and usually various trade-off decisions should be taken. Because of the reasons stated above, profound understanding of the turbine aerodynamics and aeromechanics is essential.

To this end, good deal of experimental and computational effort has been put into understanding aerodynamic characteristics of HAWTs. Numerical models based on blade element method (BEM) and their extensions which include unsteady effects are widely used because of their computational efficiency. Basic assumptions of traditional BEM include the radial independency of flow effects and two dimensional flow over the blades. Some extended BEM models include 3D effects to a certain extent and these models are accurate enough to perform preliminary force calculations coupled with structural dynamics. Thus, these models can be easily integrated to design processes leading to rather reliable wind industry. However the uncertainty of the stability calculations based on these models under random aerodynamic forcing conditions can be as high as 20%, which is unacceptable considering the growing investment costs to the wind energy industry and potential risks (AWEA, 2015).

The capability of computational fluid dynamics (CFD) tools to capture 3D effects and rotor-wake interaction is known, yet not fully validated. To have a reliable basis, dedicated experiments on HAWTs are essential to validate the existing computational tools. In the spring of 2000, a series of experiments named Unsteady Aerodynamics Experiments (UAE) were conducted by National Renewable Energy Laboratory (NREL) in the NASA Ames wind tunnel, where a 10 meter diameter, 20 kilowatt (kW) wind turbine is tested with more than 1700 turbine configurations (Fingersh et al. 2001).

There are a number of studies in literature using the data produced by NREL for validation purposes. Some authors implemented in-house/open-source solvers in these studies and compared the results with experimental data. Sorenson et al. (2002) used EllipSys3D incompressible RANS solver with k-omega SST turbulence model to investigate several upwind cases with 0 yaw angle excluding the tower and nacelle. An unstable flow behavior around 10m/s is reported in this study. The RANS code OVERFLOW-D is used by Duque et al. (2003) to predict the stall behavior and to have an insight of the fluid mechanics of the stall behavior. Well agreement with the experimental data is reported in this study. Le Pape and Gleize (2006) have implemented a low Mach number preconditioning via the Navier Stokes solver, 'elsA' to simulate the 2D airfoil and 3D blade performance. Predictions of stalled rotor torque were found to be lower than the experimental values using the k-omega SST turbulence model; however, the stall onset was well captured in these calculations. Finally Song and Perot (2014) have tried OpenFOAM on the 0° yaw angle scenario. It is reported that after 10m/s a complete stall is observed and experimental data shows a stronger stall behavior compared to the simulations. In addition to this, the torque output is significantly over-predicted for all the wind speeds.

Moreover, plenty of studies where commercial codes are implemented can be found in the literature. Mo and Lee (2011) reported that the difference of predicted and experimental torque values varied from 0.08 to 24.7% in a study where ANSYS-Fluent was used. In this study the

original NREL S809 airfoil's sharp trailing edge was modified and artificially blunted to ease the use of hexahedral grids and average y+ was reported to be around 7 for 7 m/s wind speed. Chen (2011) used ANSYS-Fluent as well to predict the behavior of the rotor under various yaw conditions, including 0°. The peak torque value was predicted as 13m/s in this study, whereas the experimental peak occurs at 10m/s. Lanzafame et al. (2003) reported an increase in the predictive capabilities of k-ω SST model when it is coupled with extra intermittency and transition Reynold's number equations. Yemule and Anjuri (2013) have used ANSYS-CFX and reported a 20% higher prediction of power at 10m/s. This is related to the difficulty of the code to capture the transitional effects at the onset of the stall. Apart from 10m/s wind speed, overall predicted power was found to be within the measurement range of experiments.

In this paper, the aerodynamics of the wind turbine in question is simulated by FlowVision under the same conditions of Unsteady Aerodynamics Experiments test sequence S. The sequence S was conducted under upwind axial in-flow condition (0° yaw angle), with a constant blade pitch of 3 degrees and constant speed of rotation of 72 RPM.

There are two aims of the current work. First is to validate the performance of the current solver in the scenario of limited computational resources (such as portable computers or weak workstations). Second is to compare the run durations of different approaches (moving reference frame, moving bodies/boundaries and sliding surfaces) to simulate the blade motion. To this end, all calculations were performed with wall function approximation and y+ values between 30 and 100 on the blade surface (y_plus area weighted average - standard deviation>30, y_plus area weighted average + standard deviation<100), except one test point, which was solved by employing an Overlapping Boundary Layer (OBL) around the blade in moving reference frame without wall function approximation (FlowVision 3.09.05 User's Guide, 2015). The resulting average y+ value was noted as 1.125 for this case. Such calculations with OBL supplement result in more than 11 million cell count and are not easy to solve by using for ordinary PCs, thus are out of the scope of the current work. Results of such calculations will be published in 'Part II' which focuses on the calculations performed on more powerful computers.

The paper is divided in the following manner: first, the computational methods are explained where the approaches to model the blade rotation, namely 'moving boundaries' and 'moving reference frame (MRF)' and 'sliding surfaces' are described together with other details such as the implemented turbulence models and computational grids' overview are given. Then, the results are compared with the data supplied by NREL, followed by a discussion of the performance of above-mentioned modeling approaches. Finally, recommendations for similar calculations to be conducted in future are given.

APPROACH

NREL Phase VI Test

NREL Phase VI test is a full scale sequence of different Unsteady Aerodynamic Experiments (UAE) with a 10.058m diameter, two-blade, tapered and twisted rotor based on S809 airfoil. The facility used for this test is the NASA-Ames wind tunnel, a 24.4m x 36.6m wind tunnel equipped with 15 bladed fans driven by electric motors. A wide scope document about the NREL Phase VI test is written by Hand et al. (2001).

Solver

The solver used in this study is commercial package FlowVision version 3.09.05. It is a C++ implemented solver based on finite-volume method and covering 3D inviscid and Navier Stokes formulation including heat transfer. It invokes Cartesian grid approach and the CAD geometries are resolved via so called "sub grid geometry resolution (SGGR)" approach. (Aksenov, 2004)

Grid (mesh) generation in this solver consists of an initial Cartesian grid generation and additional adaptations on the initial grid. The initial grid is prepared based on the preliminary requirements of the calculation and anticipated smallest cell size after the adaptations.

After the initial grid preparation, the adaptations may be applied in several ways: One may apply grid refinement based on the proximity of real geometries that are used in the calculation or imaginary objects that are specially created for adaptation purposes. One may also apply grid refinement based on the values or gradients of the flow properties obtained during the course of the calculation.

The rotor blade in this calculation is used to drive adaptation in addition to the imaginary objects encompassing the blade. Details on the grid generation are given in the Numerical Method section below.

Numerical Method

The current study focuses on validating the FlowVision solver in a limited computational resources scenario. The computations are performed in three different setups and details of the computational power are summarized in Table 1 below.

Table 1: Different Computational Setups Used

Setup #	Processor	Memory
1	Intel Core i7 4700MQ 2.4GHz	8GB
2	Intel Core i7 5820K 3.30GHz	32GB
3	Intel Xeon E5-1620 v2 3.70GHz	16GB

Within the current study, one 'moving body', one 'sliding surfaces', and nineteen 'moving reference frame' calculations were performed. In one of the frozen rotor calculations (11m/s), OBL was implemented and average y-plus on the blade surface was noted as 1.125 with a standard deviation of 1.697. All calculations except the OBL case were performed with FlowVision wall function approximation with average y-plus values between 30 and 100 on the blade surface. While wall function approximation in many solvers dictate y+ values over 30, for some specific cases FlowVision wall function can give better performance when the y+ values are above 3.5. (FlowVision 3.09.05 User's Guide, 2015)

Modeling of Blade Motion:

Different approaches, namely 'moving bodies/boundaries', 'frozen rotor' and 'sliding surfaces' are used and compared in this study.

Within the moving bodies approach any arbitrary shaped object can be defined as a moving body with 6-DOF motions determined by user-defined velocities, user-defined forces and/or fluid-induced forces. At each time step of this transient method; computational grid is obtained by automatic fitting of initial grid elements to surfaces of these moving bodies instead of motion limitations imposed by mesh morphing or regeneration.

Sliding surfaces is another transient method where one subregion, including geometry to be rotated, is assigned a rotation whereas the remaining subregion(s) is/are stationary. In this method, the grid remains stable around rotor geometry but the whole subregion rotates with respect to the absolute frame of reference.

Frozen rotor approach is a steady-state approximation analogous to freezing the rotor in a specific position and investigating the instantaneous flow field. It is based on MRF approach where governing equations are solved in a moving reference frame for a subregion or the whole computational domain.

Computational Domain:

Since the aim of the study is to reproduce the flow phenomena, the choice of the computational domain shape and size becomes an important decision. This choice should be done in such a way

that it should not be imposing unrealistic conditions on the calculation. Secondly, an excessively large computational domain would increase the computational time unnecessarily.

Based on the perception above, the computational grid for MRF is chosen as a half cylinder with a radius and length of 3.29 and 12 times the radius of the turbine respectively. For the sliding surfaces approach the full 360° model is used with same radius and length. Finally for the calculation of full model implementing moving bodies, the computational domain was restricted to 6.5m radius and 11m length since the computational resource demand for this calculation is higher. In a similar approach, Lanzafame (2013) used a cylindrical domain with a radius of 6 m and length of 11 m and reported no effect due to the relatively small domain size.

The rotor blade is imported as an *.stl file and a hub is placed to represent the geometry in the test campaign. The computational domains for different approaches are depicted in the Fig. 1. The hub is not modeled for 'moving bodies' calculation.

Since the focus is the aerodynamic performance of the rotor, the tower is neglected for all the calculations in the current study considering that the turbine in question is upwind.

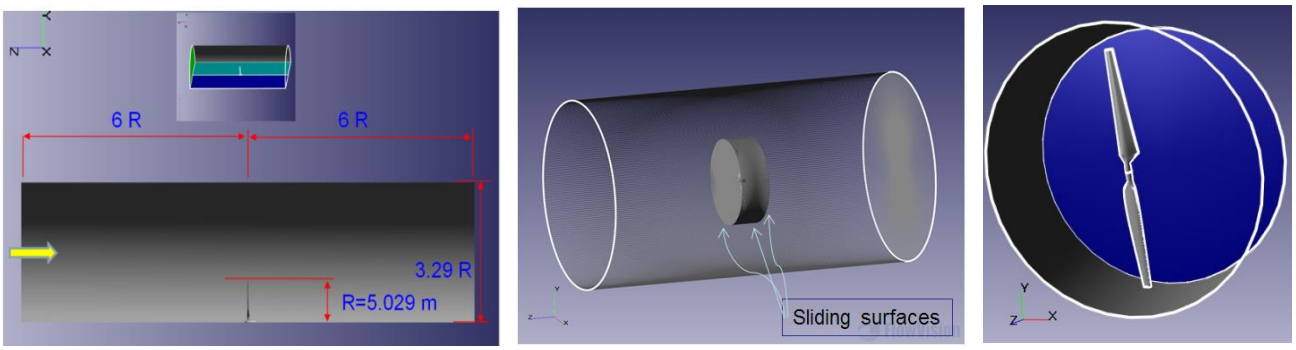

Figure 1: Computational domains used in the frozen rotor (left), sliding surfaces (center) and moving bodies/boundaries (right) calculations.

Boundary Conditions:

The problem is modeled in a half cylinder computational domain whose base contains two pairing periodic surfaces, exploiting the two fold symmetry of the test turbine. The inlet and outlet velocity boundary conditions are chosen as 'normal mass velocity' and 'constant (=reference pressure)' respectively. (FlowVision 3.09.05 User's Guide, 2015)

For different wind speeds, the turbulence intensity at the inlet is given according to the experimental findings (max. 3.26%, min. 0.21%), which can be found in the test campaign report (Hand et al. 2001). The outlet boundary condition for turbulence is given as "zero-gradient" which implies turbulence parameters in the outlet, namely the eddy viscosity, being equal to neighboring cells of outlet surface. In addition to these, the lateral surface of the cylinder is given a 'slipping' boundary condition based on the assumption that this surface is sufficiently far from the turbine and the disturbance of the turbine in the flow field in the vicinity of this surface is none or insignificant.

Turbulence Models:

FlowVision implementations of k-ε AKN and k-ω SST models are used in the current study. The k-ε AKN model, named after Abe et al. (1995), is an improved low Reynolds-number k-ε model where the velocity scale of turbulence is introduced as the friction velocity of the existing model. Gorji et al. (2013) investigated the performance of ten different turbulence models in an unsteady flow, comprising a ramp-type excursion of flow rate inside a closed channel and compared with direct numerical simulations (DNS). It is observed that k-ε AKN performed well both at lower (9308) and higher (29650) Reynolds-number cases. Although the k-ε AKN model is specific for 'low Reynolds-number' cases, it is employed in this study for comparative reasons.

The k-ω SST model is based on the assumption that in an adverse pressure gradient flow, the principal turbulent shear stress obeys the same transport equation as the turbulent kinetic energy. It was first introduced by Menter (1993, 1994) and it has been observed to perform well for the adverse pressure gradient cases by several authors (Menter, 1996; Bardina et al., 1997; Yaras and Grosvenor, 2002a and 2002b).

Solver Control:

In the solver used; time increments can be specified by entering constant time step value or, alternatively, time step can be automatically adapted by the solver at each time step depending on CFL (Courant-Friedrichs-Lewy) condition. Depending on the approach used (frozen rotor, moving body or sliding surfaces) CFL condition is defined as convective, diffusive, surface and sliding CFL, and according to these; the resulting minimum time step dictates the computation.

When time step is controlled via CFL condition, CFL=1 implies that the actual time step approaches to the explicit time step. Through the CFL criteria, the applied time step can be altered based on fluid movement (convective CFL), moving bodies (surface CFL) or sliding (sliding CFL) and gradient of the viscosity (diffusive CFL) in the flow field. Additionally, time stepping for equations like NS or energy can be individually specified. In the current study, an implicit scheme is utilized and various CFL values are tested for the sake of detecting a computationally efficient but still fairly accurate calculating configuration. (FlowVision 3.09.05 User's Guide, 2015)

A sensitivity study for CFL number is conducted by using 300, 100 and 50. For the post-stall wind speeds the oscillations were observed to be larger for CFL=300 (ratio of oscillation amplitude to mean is above 4%) case, whereas no significant difference was observed between the 100 (2.2%) and 50 (2.1%) cases. For the pre-stall wind speeds, CFL=100 and 50 did not give any oscillatory behavior, while oscillations were observed for CFL=300. Accordingly, CFL=100 is used for the frozen rotor calculations. Time step control for 'moving body' calculation is achieved through surface CFL condition, which was chosen as 1.

An implicit 'smooth reconstruction' advection scheme (2^{nd} order) is selected. The approximation of the static pressure in the cells adjacent to the blade wall is done via linear interpolation of the local pressure values.

'dynamic balance' scheme is used after each adaptation which evenly distributes the computational load over the CPUs according to their momentary capacity in order increase the calculation efficiency of each CPU and reduce the run times.

Initial Grid, Adaptations and Grid Convergence:

This section describes the generation of initial grid, adaptations applied on the initial grid and grid convergence. The software used in this work allows one to stop the calculation at any moment and delete/modify the adaptations on the initial grid or add adaptations if necessary. Thus, it was possible to perform a grid convergence study during one calculation. In order to familiarize the reader with the process, first the initial grid generation then the final adaptations used in the calculations are described. Finally grid convergence studies are presented based on these adaptations schemes.

During the initial grid generation process, the size of the nearing cells to the blade are calculated based on predicted Reynolds number and targeted y+ values. This initial value is given considering the fact that local adaptations following the initial grid generation will shrink the cells by multipliers of 2. The adaptation process is explained in detail in this section.

Since the linear velocity of the blade increases towards the tip, special care is given to this region. Accordingly, cubic cells near blade surface with 0.06m side length are created around the tip section. The side length of the initial cubic cells in the other regions of the blade was 0.10m. After 5 levels of adaptation, the final anticipated cell size with this initial grid configuration is approximately 3mm. The expansion of the cells towards the other areas in the computational domain is controlled by an expansion factor of 1.3.

Following the initial grid generation, local refinements are applied based on different criteria. In FlowVision, when an adaptation with level n is applied to the initial grid, each side of the existing cells are divided into 2^n parts (each time from their mid points) and new Cartesian cells are formed by using the division points. This process is illustrated in Fig. 2. Another important parameter of adaptations is the 'cell strata' which describes the number of layers formed with the smallest cell size obtained with the given adaptation level. For instance, if a level 1 adaptation is applied together with 'cell strata' of 3; the existing cells' sides will be divided into 2 and the resulting cells will be repeated 3 times around the adapted object.

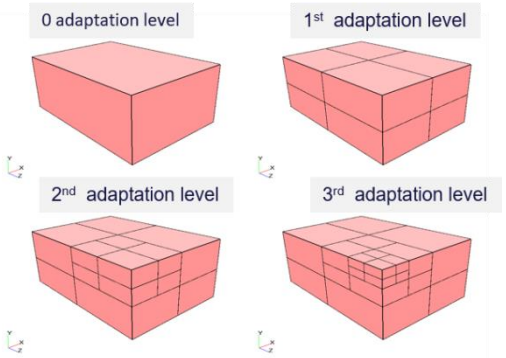

Figure 2: Illustration of FlowVision grid adaptation.

The adaptation path followed for this study consists of three different adaptation routines. First, four imaginary cylinders with different dimensions encompassing the blade are created and different adaptation levels are assigned to these cylinders. Two inner cylinders are depicted in the Fig. 3 (upper left). Second, the rotor blade itself is used as adaptation geometry. Depending on the obtained y+ values during the calculation, the adaptation level and cell strata of the rotor blade are changed and the calculations are continued. An example is shown in resulting mesh Fig. 3 (lower left). Third, for the cases where large separation is expected, automatic adaptation based on solution is employed considering the pressure and velocity gradients in the vicinity of the blade. This approach helps to automatically optimize the computational grid during the course of calculation. The maximum allowed adaptation level for 'adaptation to solution' is chosen as 5 and the maximum allowed cell count after the application of 'adaptation to solution' is limited to 6 million cells due to the limited amount of computational resources. Fig. 3 (right) depicts the resulting mesh when the adaptation to solution is given based on pressure gradient.

Table 2 below summarizes the adaptations used in the calculations and the overall cell count with and without adaptation to solution.

Table 2: Final adaptations used in the calculations and corresponding cell counts.

Adaptation Type	Within	Height (m)	Radius (m)	Adaptation Level	Cell Count
Based on Imaginary Geometries	Cylinder 1	7.5	2.2	1	3.2M
	Cylinder 2	6	1.5	2	
	Cylinder 3	5.5	0.9	3	
	Cylinder 4	5.5	0.6	4	
Based on Real Geometries	Rotor	-	-	5 with a cell Strata of 5	
Based on Pressure/Velocity Gradient	Cylinder 4	5.5	2.2	5	~5M

The grid convergence studies were performed based on the torque output. A rather low wind speed case, 7m/s, is selected since separation is not predicted for this wind speed and torque output is not expected to show a limit cycle oscillation behavior. Then the resulting mesh is used to calculate various pre and post stall wind speeds with 'adaptation to solution' (details in this section)

and the validity of the grid independence is justified. Initial grid described above is used as the base mesh. The convergence history based on torque value (half value with opposite sign, $-M_z/2$) of the 7m/s calculation is shown in Fig. 4. In the Phase 1 region, level 1 and level 3 adaptations were defined on cylinder 1 and cylinder 4 respectively.

In the Phase 2, cylinder 2 is added with a level 2 of adaptation, moreover the adaptation on the rotor was turned on with level 4 and cell strata 5. In the Phase 3, the adaptation on cylinder 4 is increased to level 4. With this configuration, the calculation was transferred to the setup #2 for further calculation.

Finally in the Phase 4, the adaptation on rotor was increased to 5 with cell strata of 5. The torque value was noted to be 753Nm for the last 30 time steps. This value is 5.9% lower than the experimental result and accepted as an accurate result when the computational resources used are considered. Thus, the Phase 4 mesh configuration is selected as the base grid for other wind speeds.

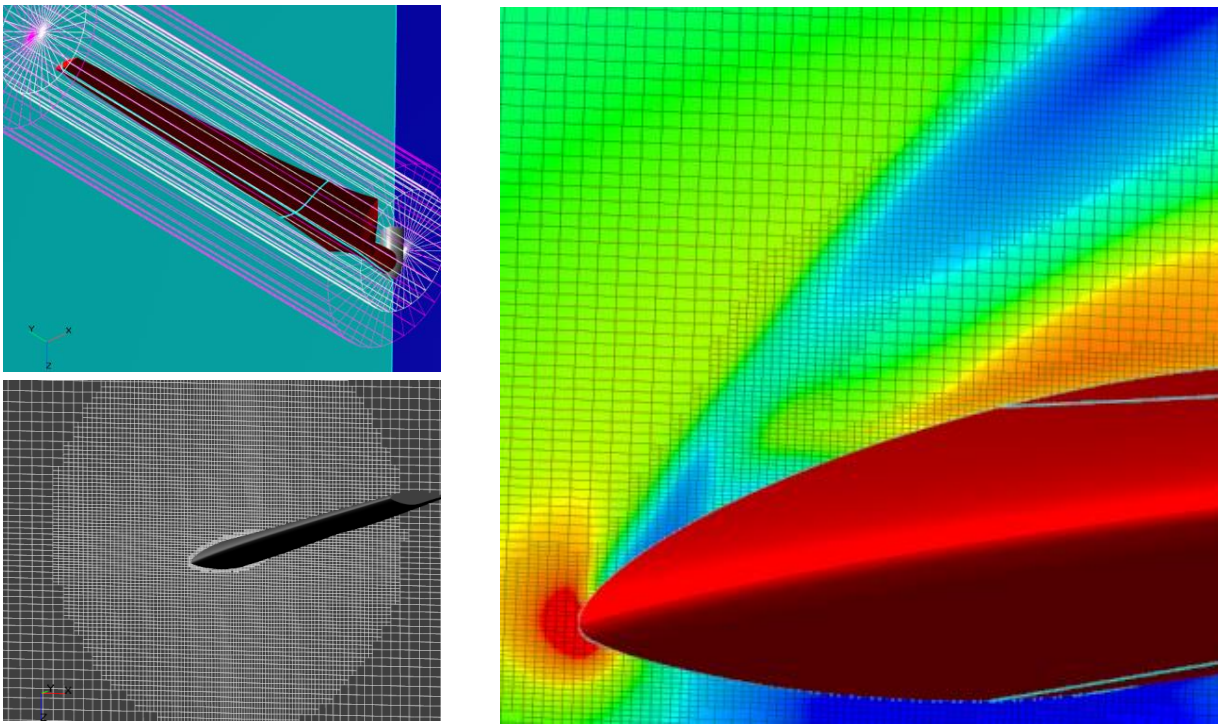

Figure 3: Imaginary cylinders for adaptation (upper left), an illustration of a mesh configuration around the rotor blade (lower left) and the mesh obtained with adaptation to solution (right) at 30% span.

The adaptation to solution option is only used in post-stall wind speeds to increase accuracy and at the same time to validate the adequacy of the Phase 4 mesh.

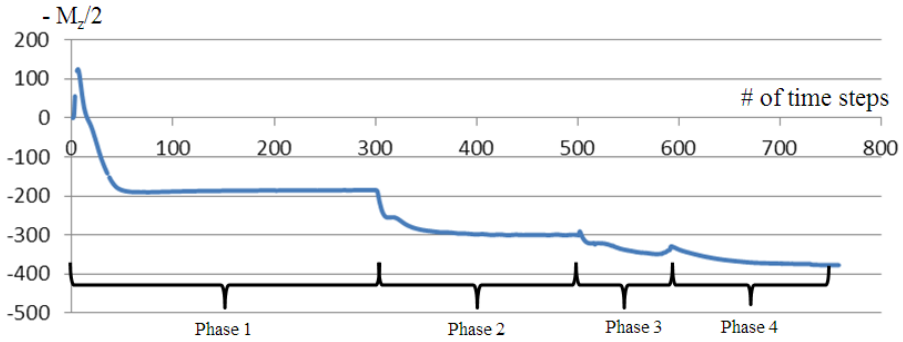

Figure 4: Convergence history of 7m/s case: Torque (half value with opposite sign) is given as a function of number of time steps.

RESULTS AND DISCUSSION

NREL Phase VI – Sequence S configuration is simulated in the scenario of low computational resources. The predicted low-speed shaft torque values are summarized in Fig. 5 together with the experimental results. While it can be said that both configurations agree with the overall shape of experimental data, k-ε AKN turbulence model show quantitative disagreement and over-predicts the stall wind speed. The maximum difference with the experimental data for these calculations is 19.5%, which occurs at 17m/s wind speed. Based on the experimental data it is possible to say that from 10m/s on it is noted that the blades are almost completely stalled. By k-ε AKN model, this behavior is only captured after 11m/s, whereas the k-ω SST model agrees well with the experimental data from this aspect. Apart from this, the predicted strength of the stall is similar with the experimental observation. These results can be correlated with few reasons. First of all, all calculations, except the OBL case at 11 m/s, were performed with wall function approximation. Unless the existing turbulence models are modified as in the work of Lanzafame (2013), it is not possible to predict this type of strong stall behavior.

The calculated torque values via k-ω SST models show better agreement than k-ε AKN model. The maximum difference for k-ω SST model is 9.22% which occurs at 11m/s. The final time steps of this calculation are shown in Fig. 5 right. As one can see, due to the nature of the stalled condition, the torque values show a limit cycle oscillation behavior. This is why time averaged results are accepted as final results for the stalled conditions. The calculation is accepted to have achieved unsteady convergence based on two criteria: (i) Algebraic residuals of all governing equations are smaller than 1e-5 and (ii) the difference between consequent peak values of torque and Cp is observed to be smaller than 1%.

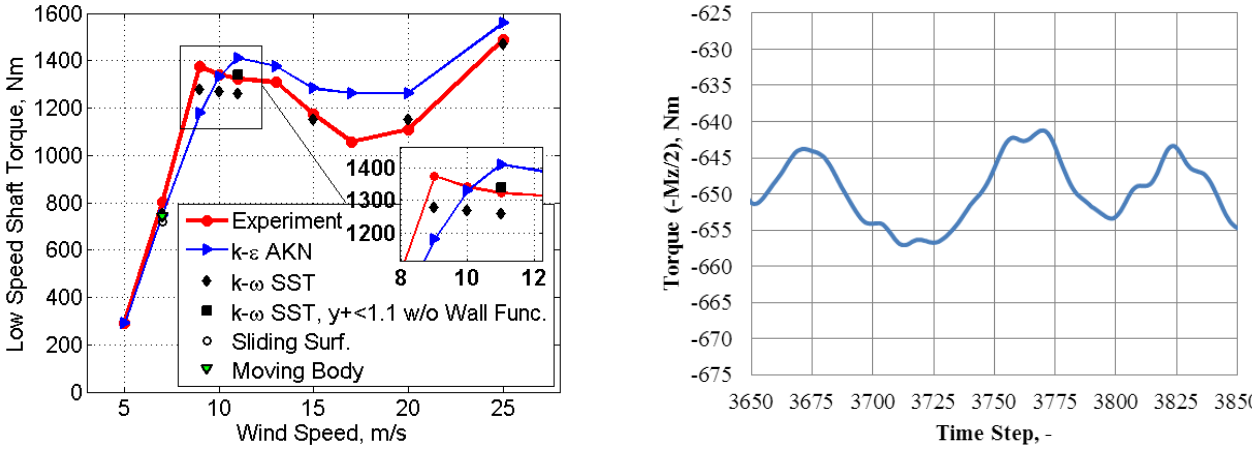

Figure 5: Comparison of experimental and predicted low speed shaft torque values (left), final time steps of 11 m/s k-ω SST (with wall func.) calculation (right).

In the Phase VI experiment, pressure distributions were measured at 0.30, 0.47, 0.63, 0.80 and 0.95 span-wise sections. Figure 6 below shows a comparison of experimental and calculated span-wise Cp distributions for k-ε AKN and k-ω SST models. It can be said that at 7m/s, both models agree with the experimental data. This is mainly because the blade functions within the design limits and there is no separation. At 13m/s, both models deviate from the experiment at 30 and 47% span. The locations where deviations from the experimental data are observed correspond to the separation locations of the blade. Due to the nature of FlowVision wall function treatment, for calculations where extreme separation phenomena may be encountered, the grid density should be high enough to keep y+ values between 3.5 and 10. In the case of current calculations with k-ω SST model at 13 m/s the y+ average is 22.6 with standard deviation of 15.6. However, further grid refinement or OBL supplement on the blade surface to obtain lower y+ values would result in too

high cell counts for the hardware used in this work which represent the capacity of small engineering enterprises. Such calculations will be dealt with in the Part II of this study.

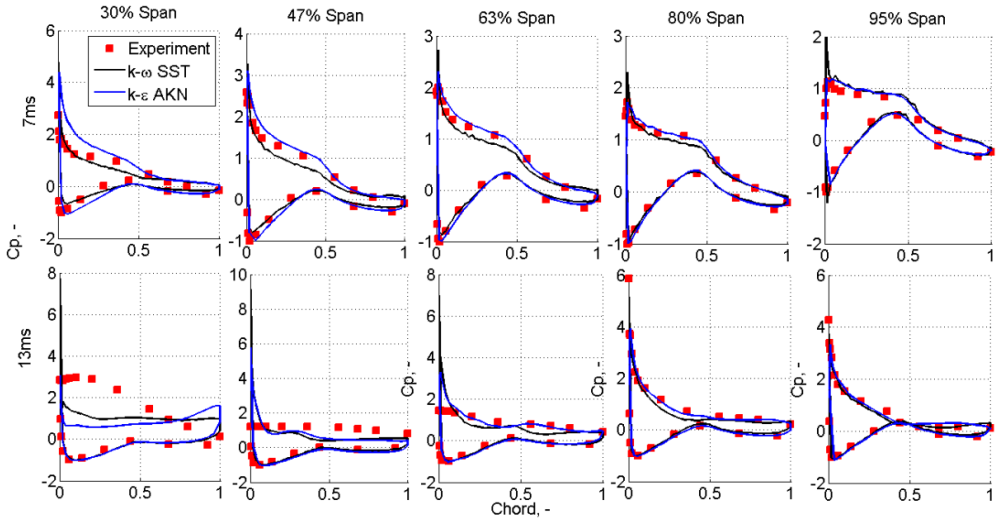

Figure 6: Cp comparison of k-ω SST and k-ε AKN models with experiment.

Computation Times:

Most of the calculations performed with cell counts between 5 and 6 million. The computation times of frozen rotor and sliding surfaces calculations were between 28 and 32 hours. The computations were started on weaker hardware setups (setup #1 and #3) with coarse grid configurations. As the adaptations are activated, they are transferred to setup #2. The details of the hardware are given in Table 1. In the final phase of calculations, the calculation time per iteration (on setup #2) varied between 100 and 130 seconds if the 'adaptation to solution' was active.

Moving body calculation was run with two blades configuration, resulting in 6.8 million cells and the total calculation time was recorded as 66 hours on the setup #2. This can be considered normal due to the nature of moving body calculations.

As an exceptional case, the frozen rotor calculation with OBL supplement consisted of 8.9 million cells and the overall computational time was noted as 102 hours on the setup #2.

The computational resource requirements for each modeling approach are summarized in Table 3. A quantity is introduced as "Normalized Resource Requirement" which represents the core-hour values of different approaches normalized by the one of Frozen Rotor.

Table 3: Resource requirements corresponding to each modeling approach.

Modeling Approach	Wall Hours	Cores	Core·hours	Normalized Resource Requirement
Moving Body	66	6	396	1.47
Frozen Rotor	45	6	270	1.00
Sliding Surface	50	6	300	1.11
Frozen Rotor + OBL	102	6	612	2.27

CONCLUSIONS

A scenario of low computational resources is created to resemble the capacity of small engineering companies and NREL Phase VI – Sequence S case is simulated employing FlowVision package version 3.09.05. Two turbulence models (k-ε AKN and k-ω SST) were employed with wall function approximations. Y+ values varied between 30 and 100 for these calculations. Comparisons of the results obtained with these turbulence models are presented. In addition to this, three different approaches to simulate the blade motion, namely; moving bodies, frozen rotor and sliding surface are used and computation times are reported.

Results show that while the k-ω SST model agrees better with the experimental findings, both of the turbulence models are capable of capturing the pre-stall behavior and both follow the general experimental torque trend as a function of wind speed. From the stall prediction perspective, the k-ω SST model agrees with the experiment, nevertheless the k-ε AKN model over-predicts the stall wind speed with 1m/s. When the predicted torque values are compared with the experimental data, it is seen that the k-ω SST model shows a better agreement for the solved cases with maximum error of 6.89% whereas the maximum error for the k-ε AKN model is 19.48% which occurs at 17m/s wind speed.

According to the CFL condition sensitivity study conducted within this work, $CFL_{convective}$=100 or lower is recommended for FlowVision if frozen rotor approach is implemented in similar calculations. If the blade motion is modeled via moving bodies approach, CFL=1 is recommended for $CFL_{surface}$.

Considering the nature of the wall functions of the solver used in this study, lowering y+ values on the blade surface might have resulted in better predictive performance; however, this does not seem possible with the selected computational resource scenario. Thus, such computationally heavier calculations with and without wall function approximations are out of the scope if the computational resources are limited and reserved for the Part II of the current study.

Looking at the computation times, it is evident that employing ‘moving bodies’ approach for simple movements such as single row blade rotation is inefficient and this approach should be reserved for more complex problems.

ACKNOWLEDGEMENTS

Authors thank Dr. Igor Moskalev and FlowVision Technical Support department for sharing their expertise.

REFERENCES

1- Renewable Energy Policy Network, (2015), *Renewables 2015 Global Status Report*
2- American Wind Energy Association, AWEA Fact Sheets, http://www.awea.org/, accessed on July 9, 2015.
3- Fingersh, L. J., Simms, D., Hand, M., Jager, D., Cotrell, J., Robinson, M., Schreck, S., and Larwood, S., "Wind Tunnel Testing of NREL's Unsteady Aerodynamics Experiment," AIAA Paper 2001-0035, 39th Aerospace Sciences Meeting, Reno, NV, Jan. 8–11, 2001.
4- Sørensen, N. N., Michelsen, J. A., & Schreck, S. (2002). Navier–Stokes predictions of the NREL phase VI rotor in the NASA Ames 80 ft× 120 ft wind tunnel. Wind Energy, 5(2-3), 151-169.
5- Duque, E. P., Burklund, M. D., & Johnson, W. (2003). Navier-Stokes and comprehensive analysis performance predictions of the NREL phase VI experiment. Journal of Solar Energy Engineering, 125(4), 457-467.
6- Le Pape, A., & Gleize, V. (2006). Improved Navier-Stokes Computations of a Stall-Regulated Wind Turbine Using Low Mach Number Preconditioning. ONERA: Tire a Part, (15), 1.
7- Song, Y., & Perot, J. B. (2015). Cfd simulation of the nrel phase vi rotor. Wind Engineering, 39(3), 299-309.
8- Mo, J. O., & Lee, Y. H. (2012). CFD Investigation on the aerodynamic characteristics of a small-sized wind turbine of NREL PHASE VI operating with a stall-regulated method. Journal of mechanical science and technology, 26(1), 81-92.
9- Chen, Y. P. (2011). A Study of the Aerodynamic Behavior of a NREL Phase VI Wind Turbine Using the CFD Methodology (Doctoral dissertation, Wright State University).
10- Lanzafame, R., Mauro, S., & Messina, M. (2013). Wind turbine CFD modeling using a correlation-based transitional model. Renewable Energy, 52, 31-39.
11- Yelmule, M. M., & Vsj, E. A. (2013). CFD predictions of NREL phase VI rotor experiments in NASA/AMES wind tunnel. International Journal of Renewable Energy Research (IJRER), 3(2), 261-269.
12- Hand, M. M., Simms, D. A., Fingersh, L. J., Jager, D. W., Cotrell, J. R., Schreck, S., & Larwood, S. M. (2001). Unsteady aerodynamics experiment phase VI: wind tunnel test configurations and available data campaigns. National Renewable Energy Laboratory, Golden, CO, Report No. NREL/TP-500-29955.
13- Abe, K., Kondoh, T., & Nagano, Y. (1995). A new turbulence model for predicting fluid flow and heat transfer in separating and reattaching flows—II. Thermal field calculations. International Journal of Heat and Mass Transfer, 38(8), 1467-1481.
14- Menter, F. R. (1993). Zonal two equation k-turbulence models for aerodynamic flows. AIAA paper, 2906, 1993.
15- Menter, F. R. (1994). Two-equation eddy-viscosity turbulence models for engineering applications. AIAA journal, 32(8), 1598-1605.
16- Menter, F. R. (1996). A comparison of some recent eddy-viscosity turbulence models. Journal of Fluids Engineering, 118(3), 514-519.
17- Bardina, J. E., Huang, P. G., & Coakley, T. (1997). Turbulence modeling validation. AIAA paper, 2121, 1997.
18- Yaras, M. I., & Grosvenor, A. D. (2002a). An Evaluation of Several Low-Re Turbulence Yaras, M. I., & Grosvenor, A. D. (2002b). Models Part 1-Flat-Plate Boundary Layer and Axisymmetric Separating Flows. ICAS 2002.
19- Numerical Simulations of Diffusing S-duct and Vortex-generator-jet Flows. 2001.
20- Aksenov, A., Dyadkin, A., Luniewski, T., & Pokhilko, V. (2004). Fluid Structure Interaction analysis using Abaqus and FlowVision. In Proc. Abaqus User Conference.
21- FlowVision 3.09.05 User's Guide: https://goo.gl/QyNPQ5, accessed on July 30, 2015.